



# Transverse mode-coupling instability with longitudinal impedance

Hai-Sheng Xu<sup>1,2</sup> · Chun-Tao Lin<sup>3</sup> · Na Wang<sup>1,2</sup> · Jing-Ye Xu<sup>1,2</sup> · Yuan Zhang<sup>1,2</sup>

Received: 19 October 2023 / Revised: 21 December 2023 / Accepted: 1 January 2024 / Published online: 18 June 2024

© The Author(s), under exclusive licence to China Science Publishing & Media Ltd. (Science Press), Shanghai Institute of Applied Physics, the Chinese Academy of Sciences, Chinese Nuclear Society 2024

## Abstract

Transverse mode-coupling instability (TMCI) is a dangerous transverse single-bunch instability that can lead to severe particle loss. The mechanism of TMCI can be explained by the coupling of transverse coherent oscillation modes owing to the transverse short-range wakefield (i.e., the transverse broadband impedance). Recent studies on future circular colliders, e.g., FCC-ee, showed that the threshold of TMCI decreased significantly when both longitudinal and transverse impedances were included. We performed computations for the circular electron–positron collider (CEPC) and observed a similar phenomenon. Systematic studies on the influence of longitudinal impedance on the TMCI threshold were conducted. We concluded that the imaginary part of the longitudinal impedance, which caused a reduction in the incoherent synchrotron tune, was the primary reason for the reduction in the TMCI threshold. Additionally, the real part of the longitudinal impedance assists in increasing the TMCI threshold.

**Keywords** Transverse mode-coupling instability · Longitudinal impedance

## 1 Introduction

Collective effects limit the highest beam current (both single and multiple bunches) in circular accelerators and essentially limit the facility’s performance. Among the numerous types of collective effects, transverse mode-coupling instability (TMCI), a type of transverse single-bunch instability, is particularly dangerous and can lead to severe particle losses.

Therefore, studies on TMCI to understand the mechanism, compute the threshold, and mitigate the instability have been conducted analytically, via simulations, and experimentally on several machines.

TMCI was first observed in PETRA and was studied by Kohaupt in 1980 [1]. The well-known “two-particle model” was proposed by Kohaupt [1] and was described in detail in Ref. [2]. The highly simplified “two-particle model” provides a clear physical picture of TMCI, using two macroparticles with opposite synchrotron oscillation phases to represent a single bunch. After obtaining the total transformation for a full synchrotron oscillation period, the stability of the two-particle system can be analyzed by computing the eigenvalues of the transfer matrix.

Additionally, a method was proposed in Refs. [3–5] to analyze the so-called strong coherent beam–beam instability in the head–tail  $\sigma$  mode. By applying this method, the stability of each colliding bunch can be analyzed by computing the eigenvalues of the one-turn transfer matrix  $M_W M_0$ , where the matrix  $M_0$  is the transfer matrix of one revolution representing the synchro-betatron motion, and  $M_W$  denotes the momentum kick generated by the beam–beam cross-wake force. Subsequently, the method was extended to include the effects of longitudinal impedance in a study on the beam–beam effect [6].

---

C. Lin: The author is now at IASF.

---

This work was supported by the National Natural Science Foundation of China (No. 12375149), the National Key R&D Program of China (No. 2022YFA1603401), and the Innovation Study of the IHEP.

---

✉ Hai-Sheng Xu  
xushs@ihep.ac.cn

✉ Chun-Tao Lin  
linchuntao@mail.iasf.ac.cn

<sup>1</sup> Key Laboratory of Particle Acceleration Physics and Technology, Institute of High Energy Physics, Chinese Academy of Sciences, Beijing 100049, China

<sup>2</sup> University of Chinese Academy of Sciences, Beijing 100049, China

<sup>3</sup> Institute of Advanced Science Facilities, Shenzhen 518107, Guangdong, China

The aforementioned methods essentially analyze bunch stability in the time domain. Moreover, the stability analyses of TMCI can also be performed in the frequency domain. The complex frequencies of the transverse coherent modes can be obtained by solving the Vlasov equation. By performing mode analyses in the frequency domain, the mechanism of TMCI can be explained by the coupling of different transverse coherent modes driven by a transverse short-range wakefield (i.e., transverse broadband impedance). When TMCI occurs, the analysis predicts violent bunch oscillation, leading to a significant particle loss during particle tracking.

Multiparticle tracking is another powerful method for studying TMCI. Several tracking codes, such as *elegant* [7] and its parallel version *Pelegant* [8], *PyHEADTAIL* [9], *mbtrack* [10] and its GPU-accelerated version *mbtrack-cuda* [11], have been developed and widely used in studies on collective instabilities, including TMCI. Compared to the aforementioned analytical methods, multiparticle tracking is more flexible and can handle more complicated situations. However, because multiparticle tracking simulates the particle motion in a beamline, many macroparticles are required to guarantee that the interaction among the particles, as well as that between the beam and environment, assimilates the real case. Furthermore, many turns are required in tracking simulations to confirm the stability of the beam.

The transverse impedance is the fundamental cause of TMCI. In previous studies, only transverse impedance was included in the study of TMCI. For example, in the classic “two-particle model” and many Vlasov solvers (such as MOSES [12], NHTVS [13], DELPHI [14], and GALACTIC [15]), linear longitudinal motion was assumed. The synchrotron oscillation frequencies were assumed to be constant within the bunch. However, this assumption is not fully self-consistent because it omits the effects of the nonlinear longitudinal motion. Nonlinear longitudinal motion can be driven by the longitudinal impedance or nonlinear RF potential, e.g., harmonic cavities [16], which are widely used in the fourth-generation synchrotron light sources [17, 18]. These factors were not considered in previous models. Harmonic cavities can lengthen the bunch and induce synchrotron-tune spread, improving beam lifetime [19–21]. In recent years, some studies have attempted to include harmonic cavity-induced nonlinear longitudinal motion [16, 22]. However, systematic studies of the influence of longitudinal impedance on TMCI are lacking.

In recent studies on the FCC-ee [23], tracking simulations observed a lower TMCI threshold when longitudinal and transverse impedances were simultaneously included. Here, we studied TMCI with and without considering longitudinal impedance using the Circular Electron Positron Collider (CEPC) storage ring lattice [24] in “Z-mode”, which has the lowest beam energy (and therefore the weakest synchrotron

**Table 1** Main Lattice Parameters of CEPC Collider Ring in “Z-Mode”

Parameters	Values
Circumference (km)	99.635
Energy, $E_0$ (GeV)	45.5
Natural emittance (nm)	0.27
Betatron tune, $\nu_x/\nu_y$	317.10/317.22
Damping partition numbers, $J_x/J_y/J_E$	1.0/1.0/2.0
Radiation damping time, $\tau_x/\tau_y/\tau_\delta$ (s)	0.81/0.81/0.40
Radiation loss per turn, (MeV)	37.36
Equilibrium energy spread (%)	0.038
Momentum compaction factor, $\eta_p$	1.43e−5
Main RF frequency, $f_{RF}$ (MHz)	652.391
Harmonic number of main RF	216,820
Bucket height, $\delta_{max}$ (%)	1.7
Peak RF voltage, $V_{RF}$ (MV)	116.66
RMS Bunch length at “zero current” (mm)	2.53
Beam pipe radius (mm)	28

radiation damping effect) among all the proposed operational modes of the CEPC collider ring. The primary lattice parameters used in these studies are listed in Table 1.

The remainder of this paper is organized as follows. In Sect. 2, the study of TMCI in the CEPC collider ring in “Z-Mode” is presented. Tracking simulations are performed under the conditions with and without the inclusion of the longitudinal impedance. In Sect. 3, the theory of TMCI is briefly reviewed, and the possible influences of the longitudinal impedance on the TMCI threshold are discussed. Systematic analyses of the influence of the longitudinal impedance are presented in Sect. 4 based on both analytical analyses and tracking results. Conclusions and a discussion are presented in Sect. 5.

## 2 Simulations of TMCI in the CEPC collider ring in “Z-Mode”

Before studying TMCI in the CEPC collider ring, obtaining a reasonable impedance model of the entire ring was necessary. During the CEPC technical design process, an impedance model [25] was gradually established owing to the development of vacuum components. Analytical formulae [26] were mainly used to compute the resistive-wall (RW) impedance, and simulations were performed for the detailed computations of the geometric impedance of complicated vacuum components. The impedance of the CEPC collider ring in the vertical direction is illustrated in Fig. 1a, where the red and blue curves represent the real and imaginary parts of vertical impedance, respectively. To show the transverse impedance data in a relatively low-frequency range,

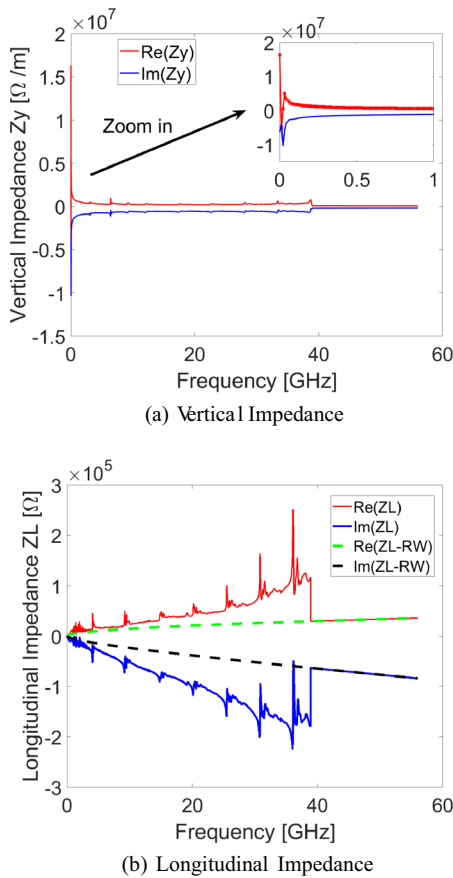


**Fig. 1** Impedance of the CEPC collider ring. **a** Indicates the total vertical impedance of the CEPC collider ring. **b** Represents the total longitudinal impedance and the longitudinal RW impedance by the solid and dashed curves, respectively. In both **a**, **b**, the solid red and blue curves represent the real and imaginary parts of the total impedance, respectively. **b**, the green and black dashed curves represent the real and imaginary parts of the longitudinal RW impedance, respectively (Color figure online)

we zoomed in on the frequency range from 0 to 1 GHz in the same figure. At present, only the transverse dipolar impedance is considered. The quadrupolar impedance has been ignored until now. The longitudinal impedances are shown in Fig. 1b, where the solid and dashed curves indicate the total longitudinal impedance and the longitudinal RW impedance, respectively. Limited by computing resources, the maximum frequencies of both the vertical and longitudinal geometric impedance of the vacuum components were set to approximately 40 GHz. However, the RW impedance was cut off at a higher frequency (approximately 56 GHz). In principle, RW impedance data can reach higher frequencies. However, truncating the RW impedance at higher frequencies does not provide a new physical picture. The limitation of the impedance model accuracy of the CEPC collider ring was the geometric impedance at that moment. More detailed

computation of geometric impedance is an important ongoing task.

In addition to impedance information, RF parameters are necessary to study TMCI. As listed in Table 1, the RF frequency was selected as 652.391 MHz. The planned bucket height was 1.7%. The corresponding peak RF voltage and synchrotron tune were approximately 116.66 MV and  $\nu_{s0} = 0.0346$ , respectively.

Systematic multiparticle simulations were performed using the elegant [7] code (and its parallel version *Pelegant*[8]) to study TMCI of the CEPC collider ring. To guarantee convergence of the simulations, 1,000,000 macroparticles were used to represent a single bunch, making the simulations very time-consuming. The total number of turns in the tracking simulation was chosen as 50,000 turns, corresponding to approximately 20 times the transverse radiation damping time. To speed up the simulations, tracking through the individual components of one revolution of the ring was simplified to using a “one-turn map”. The impedance of the entire ring was treated as a lumped component. To eliminate interference in TMCI threshold charge, neither synchrotron radiation damping, nor quantum excitation were included in the simulations presented in this section.

Simulations were performed under three different conditions to study the influence of longitudinal impedance on the threshold of TMCI. The first condition includes the vertical impedance (as shown in Fig. 1a) without considering the longitudinal impedance, which is a widely used assumption in many previous TMCI analyses. The synchrotron motion was determined under this condition using the main RF parameters listed in Table 1, which can be assumed linear at small amplitudes. The second condition considers the total longitudinal impedance of the CEPC collider ring, as indicated by the solid curves in Fig. 1b, along with the vertical impedance. The third condition includes the longitudinal RW impedance (indicated by the dashed curves in Fig. 1b) instead of the total longitudinal impedance. The original purpose of studying this situation was to supplement the first and second conditions, because the longitudinal effective impedance of the third condition was between the first and second conditions. The tracking results corresponding to the three scenarios are shown in Fig. 2 for left, middle, and right columns, respectively.

Figure 2a, b, and c show the frequency shifts of the transverse coherent modes under the three aforementioned conditions. The plots in the two lower rows show the vertical centroid oscillations (in red) and transmission rates (in blue, indicating the ratio of survival to total macroparticles) of single bunches with different charges, which could be used to indicate the TMCI threshold. Taking Fig. 2d as an example, where the single-bunch charge was set to 13 nC, no growth of the bunch centroid was observed, and the transmission rate remained at 100% in the tracking. Therefore, Fig. 2d

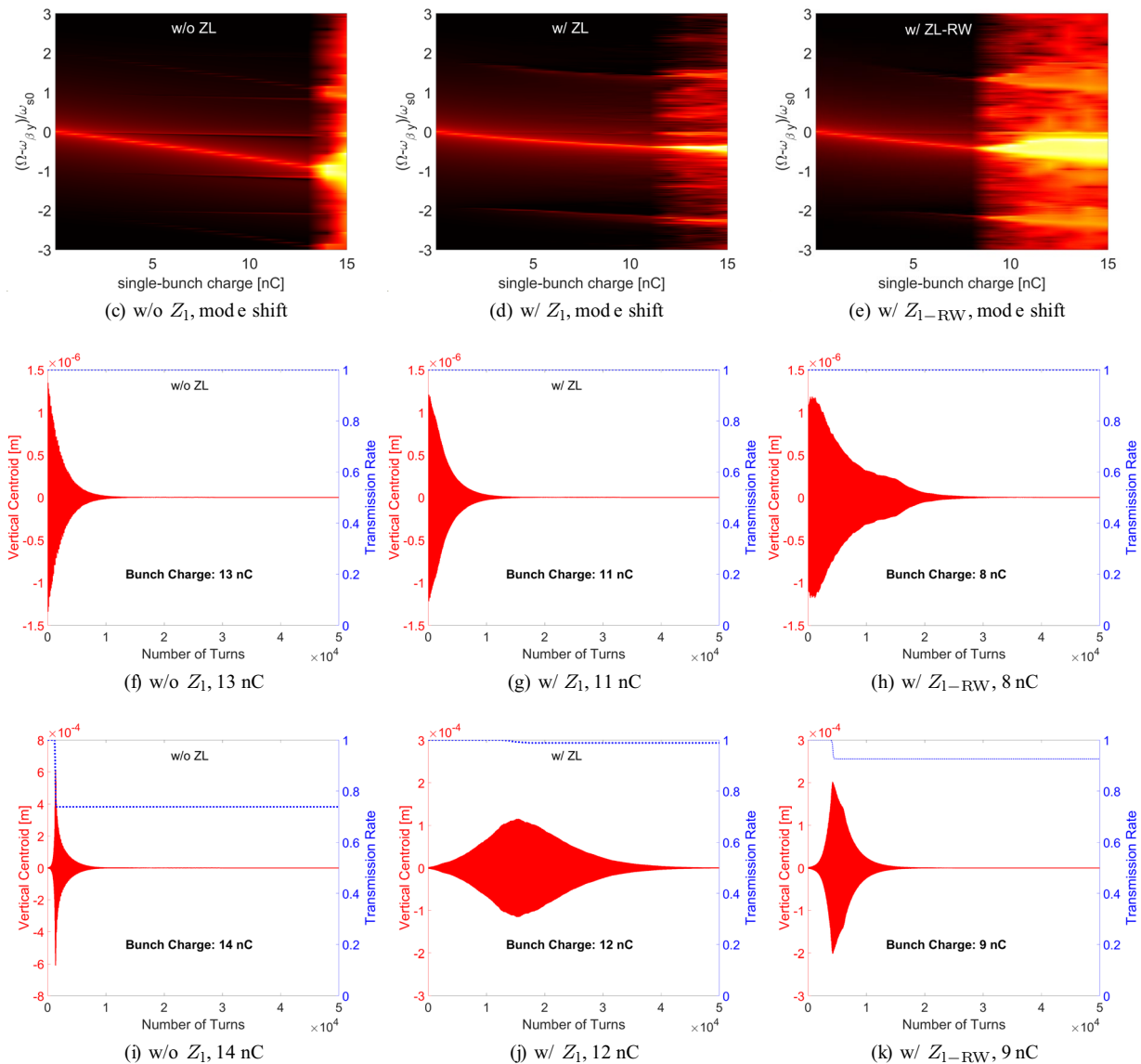


**Fig. 2** (Color online) TMCI tracking results under the conditions without longitudinal impedance (the left plots **a**, **d**, and **g**), with the total longitudinal impedance of CEPC collider ring (the middle plots **b**, **e**, and **h**), and longitudinal RW impedance (right plots **c**, **f**, and **i**). The three plots on the top row (**a**, **b**, and **c**) show the frequency shift of the transverse coherent modes under the three different conditions. The colorbar indicates the amplitude of the modes (“ $-20$ ” means the

amplitude equals to  $\log(-20)$ ). Higher values indicated that the mode was more significant. In all the pseudo-color figures in this manuscript, the meanings of the color bars are the same. Therefore, we do not repeat the explanation. The plots in the two lower rows show the vertical centroid oscillations (in red color) and the transmission rates (in blue color) of the single bunches with different charges, which are used to indicate the TMCI threshold

indicates that 13 nC/bunch is below the TMCI threshold. However, in Fig. 2g, one could see the growth of the bunch centroid, which is a clear sign of TMCI. Furthermore, remarkable particle loss was observed. Therefore, Fig. 2g indicates that 14 nC/bunch is above the TMCI threshold. The TMCI threshold charge was between 13 and 14 nC/bunch under the first condition. Similarly, we can obtain the TMCI threshold charges corresponding to the second

and third conditions in the ranges of 11–12 nC/bunch and 8–9 nC/bunch, respectively.

This can be observed by comparing the plots in the left column with the plots in the middle column (or the plots in the right column) in Fig. 2. The threshold charge of TMCI in the CEPC collider ring was higher when longitudinal impedance was not considered. Reduction in TMCI threshold current when considering longitudinal impedance in CEPC collider ring was similar to the phenomenon reported

for the FCC-ee [23]. Because the only difference was the inclusion of longitudinal impedance in the simulations, it was straightforward to guess that the effects of longitudinal impedance, such as potential well distortion, longitudinal motion characteristics, and microwave instability, must be carefully checked.

Another interesting phenomenon can be observed in Fig. 2. The TMCI threshold current was even lower with only the longitudinal RW impedance (between 8 and 9 nC) compared with the result obtained using the total longitudinal impedance (between 11 and 12 nC). However, the longitudinal RW impedance was significantly weaker than the total longitudinal impedance for the CEPC collider ring.

To better understand the physical reasons for the phenomena, we believe that it is important to examine the longitudinal dynamics of the bunch in detail. Therefore, we performed multiparticle tracking simulations using only the longitudinal impedance. Again, we used 1,000,000 macroparticles in a single bunch for tracking. The total number of turns in the tracking simulation was 50,000, which corresponds to approximately 40 damping cycles in the longitudinal direction. The obtained “final” (the word “final” indicated that the equilibrium state was reached) bunch length and energy spread, corresponding to different single-bunch charges, are shown in Fig. 3. As an increase in the energy spread can indicate microwave instability, we can observe that the threshold charges were approximately 10 nC per bunch and 40 nC/bunch, respectively, when the total longitudinal impedance and longitudinal RW impedance were considered. Interestingly, the microwave instability (MWI) threshold was lower than the TMCI threshold when using the total longitudinal impedance in the tracking simulations.

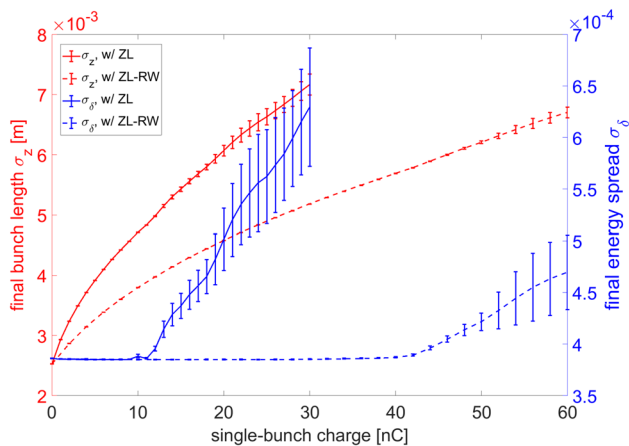


**Fig. 3** The “final” bunch length and energy spread vs. single-bunch charges when including the longitudinal total impedance and RW impedance, respectively. The shown mean values were computed by taking an average of the data from the 20,001st turn to the 50,000th turn, and the error bars were the corresponding standard derivations of the data in the same range (Color figure online)

However, when using longitudinal RW impedance in the simulations, the obtained TMCI threshold was lower than the MWI threshold. This difference allowed us to check whether MWI affects transverse stability. Furthermore, this phenomenon means that it would be more suitable to use the longitudinal RW impedance in analytic analyses of TMCI. Otherwise, the unstable longitudinal motion is difficult to treat analytically.

### 3 TMCI theory

The basic methods to determine the TMCI threshold using the “two-particle model” and by solving the Vlasov equation are briefly discussed in the Introduction section. In this section, we review the two methods in more detail.

The ingeniousness of the “two-particle model” is to divide one full synchrotron period into two halves to ensure that the “leading particle” and the “trailing particle” will not exchange positions in each half of the synchrotron period. Therefore, in the first half of the synchrotron period, the equation for the betatron motion of the leading particle (marked as No. 1) describes the free betatron oscillations. Meanwhile, the transverse kick generated by the wakefield of the leading particle is included in the equation for the betatron motion of the trailing particle (marked as No. 2). In the second half of the synchrotron period, the positions of these two particles exchange, indicating that particle No. 2 becomes the leading particle. Therefore, the equations of the betatron motion can be written similarly as in the first half-synchrotron periods. After obtaining the total transformation for the full synchrotron oscillation period, the stability of the two-particle system can be analyzed by computing the eigenvalues of the transfer matrix. The stability criterion obtained from the “two-particle model” is expressed as follows [2]

$$Y = \frac{\pi N_b r_e W_0 c^2}{4\gamma C \omega_\beta \omega_s} \leq 2, \tag{1}$$

where  $Y$  is a dimensionless parameter,  $N_b$  is the number of electrons per bunch,  $r_e$  is the classical electron radius,  $W_0$  is the assumed transverse constant wake,  $c$  is the speed of light in vacuum;  $\gamma$  is the Lorentz factor;  $C$  is the circumference of the ring; and  $\omega_\beta$  and  $\omega_s$  represent the angular frequencies of betatron motion and synchrotron oscillation, respectively.

It can be seen from Eq. (1) that the TMCI threshold predicted by the “two-particle model” is proportional to the betatron frequency, synchrotron frequency, and beam energy and the circumference of the ring and is inversely proportional to the strength of the transverse wakefield. The TMCI study of the CEPC collider ring determined the betatron frequency, beam energy, circumference, and transverse wakefields,

implying that more attention should be paid to the synchrotron frequency.

Analyzing the TMCI threshold by solving the Vlasov equation essentially computes the complex frequencies of the transverse coherent modes. The starting point is the bunch distribution  $\phi$  in 4-D phase space (either in the polar coordinate phase space  $(q, \delta, r, \phi; s)$ , or equivalently,  $(y, p_y, z, \delta; s)$ )

$$\psi = f_0(q)g_0(r) + f_1(q, \theta)g_1(r, \phi)e^{-i\Omega s/c} \tag{2}$$

where  $\Omega$  is the complex mode frequency and  $f_0$  and  $f_1$  ( $g_0$  and  $g_1$ ) are the unperturbed and perturbed transverse (longitudinal) beam distributions, respectively, satisfying the Vlasov equation

$$\frac{\partial \phi}{\partial s} + y' \frac{\partial \phi}{\partial y} + p'_y \frac{\partial \phi}{\partial p_y} + z' \frac{\partial \phi}{\partial z} + \delta' \frac{\partial \phi}{\partial \delta} = 0 \tag{3}$$

where the prime represents the derivative with respect to the independent variable  $s$ , for example,  $y' = dy/ds$ . Here, TMCI is considered to have zero chromaticity. Assuming that only transverse motion is affected by the transverse wake force; however, the synchrotron motion is not perturbed, the Eq. (3) is reduced to an infinite set of equations [2]

$$\begin{aligned} (\Omega - \omega_\beta - l\omega_s)\alpha_l R_l(r) &= -i \frac{\pi r_0 \omega_s}{\gamma \omega_\beta T_0^2 \eta} g_0(r) \\ &\times \sum_{l'=-\infty}^{\infty} \int_0^{\infty} r' dr' \alpha_{l'} R_{l'}(r') i^{l-l'} \\ &\times \sum_{p=-\infty}^{\infty} Z_y^\perp(\omega') J_l\left(\frac{\omega' r}{c}\right) J_{l'}\left(\frac{\omega' r'}{c}\right) \\ l &= 0, \pm 1, \pm 2, \dots, \end{aligned} \tag{4}$$

where  $Z_y^\perp(\omega')$  denotes the transverse impedance in  $y$  direction with  $\omega' \equiv p\omega_0 + \omega_\beta + l\omega_s$ .  $\alpha_l, R_l(r)$  are the Fourier coefficients of  $g_1(r, \phi)$  and  $g_1(r, \phi) = \sum_{l=-\infty}^{\infty} \alpha_l R_l(r) e^{il\phi}$ . Analytical studies eventually lead to eigenvalue problems. The real and imaginary parts of the eigenvalues  $\Omega$  provide information on mode frequency and growth rate. When the bunch intensity was low,  $\Omega$  could be determined. As the intensity increased, the oscillation frequencies of some modes (usually the lowest-order mode, called the 0 mode) shift toward other modes. Above a threshold current, the two modes couple, and the bunch becomes unstable.

Using the ‘‘air-bag model’’ to represent the longitudinal bunch distribution  $g_0(r)$ , the scaling for the instability threshold  $N_{th}$  is approximately

$$N_{th} \propto \omega_s \omega_\beta E. \tag{5}$$

From Eq. (5), the ‘‘mode-coupling model’’ gives the same trend as the ‘‘two-particle model,’’ which is the higher TMCI threshold charge that can be expected if any value among the

synchrotron frequency, betatron frequency, and beam energy can be increased. Similar to the aforementioned analysis of the ‘‘two-particle model,’’ this method demonstrates the importance of synchrotron frequency.

## 4 Analyses with longitudinal impedance

### 4.1 Development of the analytic method

As mentioned above, a method to analyze the stability of colliding bunches is to compute the eigenvalues of the matrix product of the synchro-betatron transfer matrix  $M_0$  and the matrix  $M_w$ , which represents the momentum kick induced by the beam–beam cross-wake force. This method was developed in Ref. [3, 4]. The method was then extended to include the longitudinal impedance in a study on the beam–beam effect [6]. In the following text, we mainly follow the procedure proposed in Ref. [6] to develop an analytical method for analyzing TMCI considering longitudinal impedance.

TMCI in the horizontal and vertical directions is usually studied separately. In the following section, the vertical direction is considered as an example. Vertically normalized coordinates  $(Y, P_y)$  instead of the vertical phase-space coordinates  $(y, p_y)$  were used in the following computations. The normalized coordinates  $(Y, P_y)$  can be expressed as

$$Y = y/\sqrt{\beta_y}, \quad P_y = p_y \cdot \sqrt{\beta_y} + \alpha_y \cdot y/\sqrt{\beta_y}, \tag{6}$$

where  $\alpha_y$  and  $\beta_y$  are Courant-Snyder parameters. For simplicity, in the following analyses, we assume that the vertical wake force is lumped at the position where  $\alpha_y = 0$ .

The vertical coordinates of the particles  $(Y, P_y)$  are functions of the longitudinal phase-space coordinates. To proceed with our analysis, we use the longitudinal action-angle variables  $(J, \phi)$  instead of  $(z, \delta)$  phase-space coordinates to represent the vertical coordinates of the particles (i.e.,  $Y = Y(J, \phi)$  and  $P_y = P_y(J, \phi)$ ).  $z$  and  $\delta$  denote the relative longitudinal position and energy spread, respectively. The two sets of phase-space coordinates are related by Lee [27]:

$$J = \frac{1}{2\pi} \oint \delta dz, \quad \phi = \frac{\partial F_2(z, J)}{\partial J}, \tag{7}$$

where  $F_2(z, J)$  is the second-type generating function defined as follows:

$$F_2(z, J) = \int^z \delta(J, z') dz'. \tag{8}$$

Because  $Y(J, \phi)$  and  $P_y(J, \phi)$  are periodic functions of  $\phi$  with a period of  $2\pi$ , we can expand the expression of the normalized coordinates azimuthally to obtain

$$Y(J, \phi) = \sum_{l=-\infty}^{\infty} Y_l(J)e^{il\phi}, \quad P_y(J, \phi) = \sum_{l=-\infty}^{\infty} P_l(J)e^{il\phi}. \quad (9)$$

Transfer matrix  $M_0$  to the transform vector

$$(Y_l(J), P_l(J)), \quad (10)$$

per revolution without wakefield can be written as

$$M_0 = e^{-i2\pi\nu_s(J)} \begin{pmatrix} \cos \mu_y & \sin \mu_y \\ -\sin \mu_y & \cos \mu_y \end{pmatrix}, \quad (11)$$

where  $\mu_y = 2\pi\nu_y$ ,  $\nu_y$  is the vertical tune.  $\nu_s(J)$  is the synchrotron tune expressed as a function of  $J$ . Under conditions without consideration of longitudinal impedance and assuming that the particles experience small-amplitude synchrotron oscillations at a single frequency RF system (where the synchrotron oscillation can be simplified as a simple harmonic oscillator), the synchrotron tune can be treated as a constant value for different  $J$  (i.e.,  $\nu_s(J) = \nu_{s0}$ ). However, when we include the longitudinal impedance,  $\nu_s$  in Eq. (11) varies according to  $J$ , indicating that the spread of synchrotron tune can be included in the analyses of transverse stability (TMCI). In addition, considering the longitudinal impedance, the particle’s trajectory in the longitudinal phase space is distorted from an ellipse and can be any shape. As discussed later, this distortion can also be included in the analysis.

Furthermore, one must consider that the transverse wakefield generated by the leading particles acts on trailing particles as they move along the accelerator. As mentioned previously, the vertical impedance of the entire ring was lumped into one location, providing a vertical momentum kick to the particles at each revolution. This vertical momentum kick can be expressed as [2]

$$\Delta p_y = -\frac{N_b r_e}{\gamma} \int_{-\infty}^{\infty} y(z)W_y(z-z')\rho(z')dz'. \quad (12)$$

Using  $\rho(z') = \int \psi(J', \phi')d\delta'$ , where  $\psi(J, \phi)$  is the particle longitudinal phase-space distribution, and the normalized variables defined in Eq. (6), we rewrite the equation in terms of  $(J, \phi)$

$$\Delta P_y(J, \phi) = -\frac{N_b r_e \beta_y}{\gamma} \int_0^{\infty} dJ' \int_0^{2\pi} d\phi' \times W_y(z-z')Y(J, \phi)\psi(J', \phi')\rho(z'), \quad (13)$$

where  $z = z(J, \phi)$ ,  $z' = z(J', \phi')$ . We assume that the longitudinal phase-space distribution is stationary; thus,  $\psi(J, \phi)$  is only a function of  $J$ , that is,  $\psi(J, \phi) = \psi(J)$ . In this study, we chose the smooth accelerator model, and the value of  $\beta_y$  was  $\beta_y \approx R/\nu_y$ , where  $R$  is the average radius of the storage ring. Substituting the expansion of Eqs. (9) into (13), multiplying

$e^{-il\phi}$  on both sides, and integrating  $\phi$  from 0 to  $2\pi$ , we obtain the momentum kick for each azimuthal mode  $P_l(J)$  induced by the transverse wakefield

$$\Delta P_l(J) = -\frac{\beta_y}{2\pi} \sum_{l'} \int dJ' W_{ll'}(J, J')\psi(J')Y_{l'}(J'), \quad (14)$$

where

$$W_{ll'}(J, J') = \frac{N_b r_e}{\gamma} \iint d\phi d\phi' e^{-il\phi + il'\phi'} W_y(z-z'). \quad (15)$$

$W_{ll'}(J, J')$  can be regarded as a weight function that describes the interaction strength between the two azimuthal modes  $l, l'$  of the two different action particles  $J, J'$ .

After synchro-betatron transformation of Eq. (11) and the momentum kick of Eq. (14) induced by wakefield, we attempt to determine the stability of the circulating bunches. The objective was to obtain the eigenvalues of the transformations. To achieve this, we first truncated the infinite summation  $l$  of Eq. (9) at  $\pm l_{\max}$ . Then, we discretized and sampled continuous variables  $J$  at specific values  $J_i, i = 1, 2, \dots, n_j$ , where  $n_j$  is the number of grids [28]. The transferred dipole-moment vector in Eq. (10) becomes

$$(Y_l(J_i), P_l(J_i)), \quad (16)$$

where  $l = 0, \pm 1, \pm 2, \dots, \pm l_{\max}$ ,  $J = J_1, J_2, \dots, J_{n_j}$ . The length of this vector was  $2 \times n_j \times (2l_{\max} + 1)$ . Therefore, the synchro-betatron transformation and momentum kick from the transverse wakefield for vector (16) can be written directly from Eqs. (11) and (14),

$$M_0 = e^{-2\pi i \nu_s(J_i)} \begin{pmatrix} \cos \mu_y & \sin \mu_y \\ -\sin \mu_y & \cos \mu_y \end{pmatrix}, \quad (17)$$

and

$$\Delta P_l(J_i) = \sum_{l'} \sum_{l''} M_{ll'l''} Y_{l''}(J_{i'}), \quad (18)$$

where

$$M_{ll'l''} = -\frac{\beta_y}{2\pi} \Delta J_{i'} W_{ll'}(J_i, J_{i'})\psi(J_{i'}). \quad (19)$$

For the transverse wake function  $W_y(z)$  of a real machine, the weight function  $W_{ll'}(J_i, J_{i'})$  in (15) can assume an arbitrary form. Therefore, the integration of  $\phi$  takes the form of a discrete summation

$$W_{ll'}(J_i, J_{i'}) = \frac{N_b r_e}{\gamma} \sum_j \sum_{j'} e^{-il\phi_j + il'\phi_{j'}} \times W_y(z(J_i, \phi_j) - z(J_{i'}, \phi_{j'})) \Delta\phi_j \Delta\phi_{j'}. \quad (20)$$

The transverse wakefield kick in Eq. (18) can be written in a more intuitive matrix form as

$$M_W = \begin{pmatrix} 1 & 0 \\ M_{il'j'} & 1 \end{pmatrix}. \tag{21}$$

This matrix can be regarded as a thin-lens quadruple with different focal lengths for different particles and azimuthal modes.

Finally, the total one-turn transfer matrix is  $M_0 M_W$  with dimensions of  $(2 \times n_J \times (2l_{\max} + 1))^2$ . The stability of the revolving beam was determined using eigenvalues ( $\lambda$ 's) of  $M_0 M_W$ .

To perform the analysis of TMCI using the aforementioned method, according to Eqs. (17) and (18), the synchrotron tune  $\nu_s(J)$  and particle longitudinal phase-space distribution  $\psi(J)$  at equilibrium state is needed. This can be obtained from the single-particle Hamiltonian by considering the longitudinal impedance (wakefield),

$$H = -\frac{\eta_p}{2} \delta^2 - \frac{\mu_z^2}{2\eta_p C^2} z^2 + \frac{1}{C} \frac{N_b r_e}{\gamma} \int_0^z dz'' \int_{-\infty}^{\infty} dz' W_z(z'' - z') \rho(z'). \tag{22}$$

where  $\eta_p$  is the phase slippage factor,  $C$  is the circumference of the ring,  $\mu_z = 2\pi\nu_s$  is the synchrotron phase advance per revolution,  $W_z(z)$  is the longitudinal wakefield (pseudo-green function or short-bunch wake potential). Owing to the synchrotron radiation damping and quantum excitation, the equilibrium distribution is in  $\delta$  is considered Gaussian with an RMS value  $\sigma_\delta$ ,

$$\psi(z, \delta) = \frac{1}{\sqrt{2\pi}\sigma_\delta} \exp\left(-\frac{\delta^2}{2\sigma_\delta^2}\right) \rho(z). \tag{23}$$

The equilibrium longitudinal bunch distribution  $\rho(z) = \rho_{\text{eq}}(z)$  can be computed either numerically by solving the Haïssinski equation or by multiparticle tracking simulations. The detailed process to solve the Haïssinski equation is not discussed in this paper because it has been presented in many previous publications, for example, [29–31].

We can then substitute the equilibrium longitudinal bunch distribution  $\rho_{\text{eq}}(z)$  into Eq. (22) to obtain the expression of the “equilibrium” Hamiltonian  $H_{\text{eq}}$ . The Hamiltonian tori corresponding to the given values of the oscillation amplitudes  $z_{\text{amp}}$  (i.e.,  $J$ ) can be obtained numerically based on  $H_{\text{eq}}$ . It is then straightforward to extract the information of  $\nu_s(J)$  by numerically solving the mapping equations of the longitudinal motion using the standard method provided in textbooks, for instance, in Refs. [27, 32].

The same process can be applied to the study without considering longitudinal impedance except for solving the Haïssinski equation.

### 4.2 Study of the TMCI both analytically and by simulations

Using the analytical method, the TMCI can be studied with and without consideration of the longitudinal impedance. To benchmark the analytical method, a TMCI study was conducted under conditions without a longitudinal impedance. The mode angular frequency  $\Omega$  and the growth rate are given by  $\omega_0/(2\pi) \cdot \tan^{-1}(\text{Im}(\lambda)/\text{Re}(\lambda))$  and  $\log \lambda$ , respectively. A comparison of the analytical and tracking results is presented in Fig. 4a, where a pseudo-color plot is obtained via multiparticle tracking, as shown in Fig. 2a, and the white dots are computed using the aforementioned analytical method. The analytical results indicate that the two lowest modes ( $l = 0$

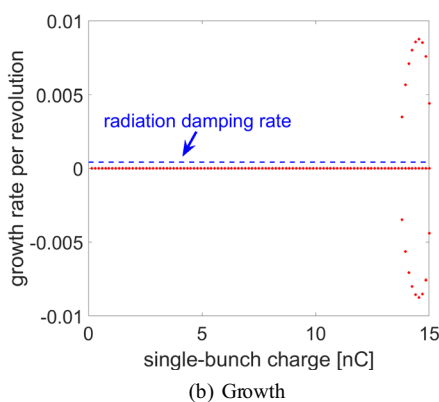
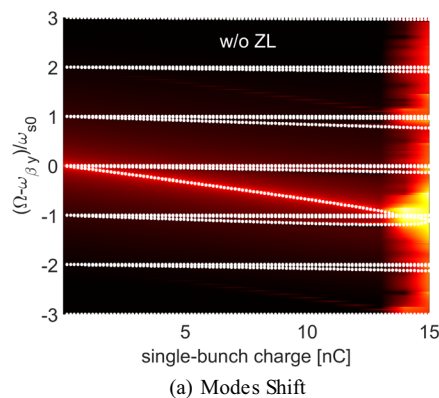


**Fig. 4** (Color online) TMCI analyses without longitudinal impedance. **a** represents the betatron frequency shift, indicating the shift and coupling of the head–tail modes. The pseudo-color plot was the result of the multiparticle tracking. The white dots were obtained using the analytic method. The red dots given in **b** were the growth rates of the modes at different single-bunch charges. The blue dashed line in **b** indicated the synchrotron radiation damping rate

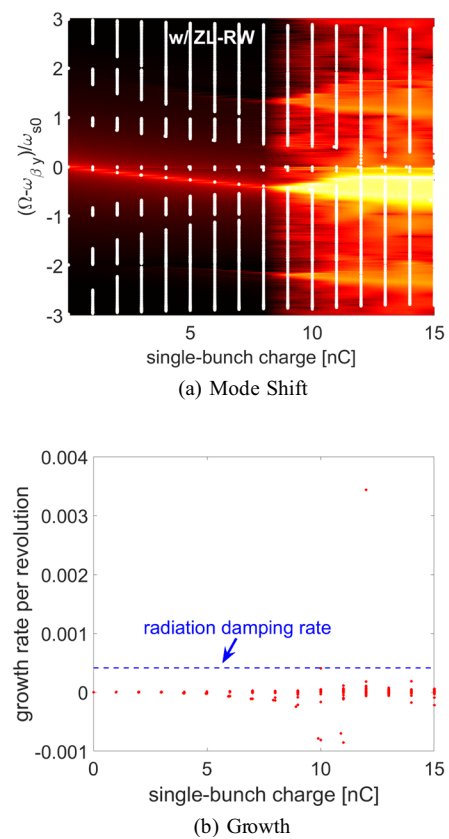
and  $l = -1$ ), coupled at approximately 13–14 nC/bunch, exhibited excellent agreement with the tracking results.

Furthermore, the growth rates of TMCI are indicated by the red dots in Fig. 4b. We observed that the growth rate remained at zero when the single-bunch charge was below approximately 13 nC and became nonzero when the single-bunch charge was above 14 nC. This is consistent with the mode-coupling analyses presented in Fig. 4a. Furthermore, the blue dashed lines in Fig. 4b indicates the synchrotron radiation damping. The growth rate was compared to that of the synchrotron radiation damping rate, we determined whether the bunch was stable.

In Fig. 4a, excellent agreement between the analytical analysis and multiparticle tracking simulations without considering the longitudinal impedance is shown. In the next step, we do not assume linear synchrotron motion in the longitudinal direction. Instead, the longitudinal impedance was included in the TMCI study. The longitudinal equilibrium distribution was obtained by considering the longitudinal impedance.

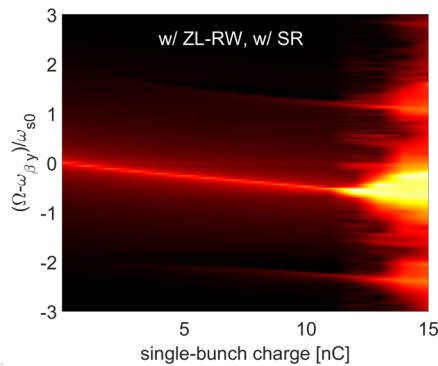
However, as presented in Sect. 2 or, more precisely, in Figs. 2b and 3, when the longitudinal impedance of CEPC (the red and blue curves in Fig. 1b), the MWI threshold charge was lower than the TMCI threshold. Since no equilibrium Haissinski solution exists above the MWI threshold, the corresponding longitudinal bunch distribution change turn after turn, making the analytic analysis of TMCI impossible. Figures 2c and 3 show that MWI threshold charge is much higher than the TMCI threshold charge when using the longitudinal RW impedance (green and black dashed curves in Fig. 1b), indicating that the equilibrium longitudinal distribution always exists when studying TMCI considering longitudinal RW impedance. Therefore, we use the longitudinal RW impedance (green and black dashed curves in Fig. 1b) in the TMCI studies. The computational results are presented in Fig. 5.

Figure 5a shows excellent agreement between the analytical and tracking results when the longitudinal RW impedance is included. Furthermore, the threshold charge predicted by the tracking simulations corresponds to the position where  $l = 0$  and  $l = -1$  modes are coupled, as predicted by the analytical analyses. It is interesting to note the following analytical results predicted that the spread of each azimuthal mode (corresponding to the indices of the vertical axis  $(\Omega - \omega_{\beta_y})/\omega_s$ ) increases as the single-bunch charge increases. Therefore, couplings between the higher-order modes below the threshold charge correspond to the coupling between  $l = 0$  and  $l = -1$  modes. For instance, the coupling between  $l = 2$  and  $l = 3$ -modes and coupling between the  $l = -3$  and  $l = -2$  modes occurred in the ranges of approximately 3 and 4 nC/bunch. Moreover, the coupling between  $l = 1$  and  $l = 2$  modes and the coupling between  $l = -2$  and  $l = -1$  modes occurred in the range of



**Fig. 5** (Color online) TMCI analyses with longitudinal RW impedance. **a** represents the betatron frequency shift, indicating the shift and coupling of the head–tail modes. The pseudo-color plot was the result of the multiparticle tracking. The white dots were obtained using the analytic method. The red dots given in **b** were the growth rates of the modes at different single-bunch charges. The blue dashed line in **b** indicated the synchrotron radiation damping rate

approximately 7 and 8 nC/bunch. However, no instability was observed, corresponding to the coupling of the aforementioned higher-order modes in the multiparticle tracking. It can be seen in Fig. 5b the growth rate was already nonzero at approximately 6 nC/bunch. However, the growth was slow at a relatively low charge (e.g., 6 nC/bunch). Considering the low growth rate and finite number of turns in the tracking simulations, growth is not easily observed from the tracking results; for example, the pseudo-color plot in Fig. 5a. Furthermore, by comparing analytic results of the growth rate and the synchrotron radiation damping rate, it can be seen that the growth rate below approximately 12 nC/bunch is smaller than the synchrotron radiation damping rate. Therefore, we predict that if we include synchrotron radiation effects in the tracking simulations, the obtained threshold should be in the range of 11 and 12 nC/bunch. The tracking results considering the longitudinal RW impedance and synchrotron radiation effects are shown in Fig. 6, which confirms the prediction using simulations.



**Fig. 6** (Color online) TMCI analyses with longitudinal RW impedance and synchrotron radiation effect via multiparticle tracking

### 4.3 Influences of the real and imaginary parts of the longitudinal impedance

The studies showed that longitudinal impedance leads to a reduction in the TMCI threshold. Furthermore, it was confirmed that both the developed analytical method and multiparticle tracking can be used to investigate this phenomenon. In this study, we conducted systematic investigations into the underlying physics.

The first question we aimed to understand is how the real and imaginary parts of the longitudinal impedance affect the TMCI. It would be of great significance to know the answer because this may guide more precise optimization of the longitudinal impedance.

The studies were first conducted using multiparticle tracking by including either the real part of the total longitudinal impedance (red solid curve in Fig. 1b) or the imaginary part of the total longitudinal impedance (solid blue curve in Fig. 1b). The total number of turns in the tracking process is 50,000. Synchrotron radiation effects were not considered in this study. The mode frequency shifts corresponding to these two conditions are shown in Fig. 7.

Compared with the results obtained for the entire longitudinal impedance (shown in Fig. 2b), the TMCI threshold charge increases when only the real part of the longitudinal impedance is included. However, the TMCI threshold decreased significantly when only the imaginary part of the longitudinal impedance was included in tracking. We first performed tracking simulations in the longitudinal direction to determine the reason. The same settings were used as those described above. The obtained “final” bunch lengths and energy spreads are shown in Fig. 8a, b.

It can be seen in Fig. 8, the purely imaginary longitudinal impedance causes bunch lengthening as the single-bunch charge increases, without driving MWI. Moreover, the simulations demonstrated that the purely real longitudinal impedance was responsible for the MWI, significantly

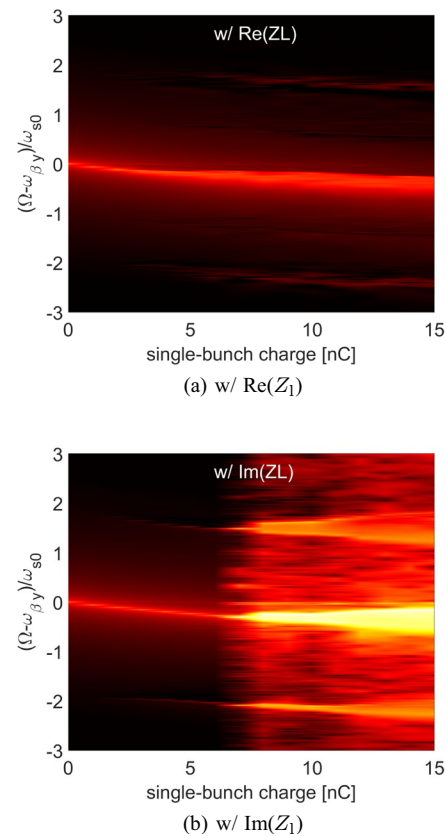


**Fig. 7** (Color online) Modes frequency shift vs. single-bunch charge. **a, b** were obtained with the consideration of the real part and imaginary part of the longitudinal impedance, respectively. 50,000 turns were used for the tracking. The synchrotron radiation effects were not included

reducing the MWI threshold. No significant increase in bunch length was observed below the threshold current with only the real longitudinal impedance. However, the bunch lengthened as MWI occurred. In general, as shown in Fig. 8a, the bunch lengths under the three different conditions were not significantly different for a relatively large range of bunch charges, for instance, from 5 to 15 nC/bunch. The charge densities corresponding to the same single-bunch charge should not differ significantly under these three conditions. More detailed information needs to be obtained by carefully analyzing the bunch distributions and the corresponding incoherent synchrotron tune at different single-bunch charges when the total longitudinal impedance  $Z_1$ , purely real longitudinal impedance  $\text{Re}(Z_1)$ , and purely imaginary longitudinal impedance  $\text{Im}(Z_1)$  are used. The results are shown in Fig. 9.

Figure 9 clearly shows that the real part of the longitudinal impedance causes a shift in the longitudinal centroid positions and head–tail asymmetry, which indicates that particles lost energy, and potential well distortion

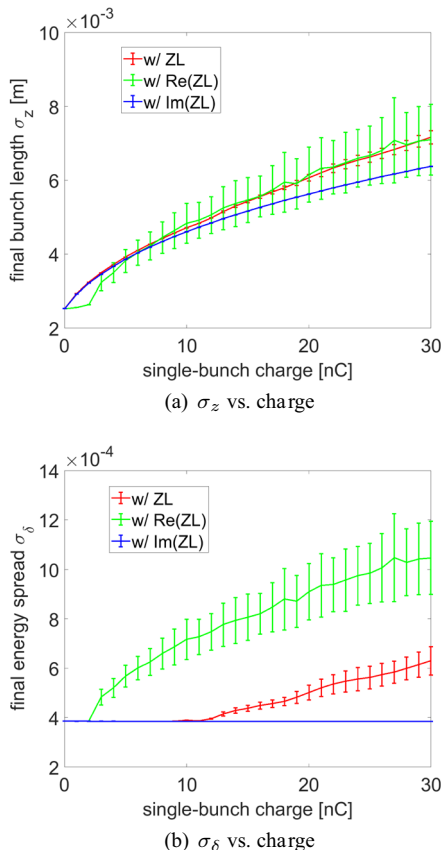


**Fig. 8** (Color online) Final bunch length (in **a**) and energy spread (in **b**) under the following three different conditions: the first condition is with both the real and imaginary parts of the total longitudinal impedance shown by Fig. 1b, the second condition is with only the real part of the total longitudinal impedance, and the third condition is with only the imaginary part of the total longitudinal impedance. The shown mean values were computed by taking an average of the data from the 20,001st turn to the 50,000th turn, and the error bars were the corresponding standard derivations of the data in the same range

occurred because of the real longitudinal impedance, but no incoherent synchrotron-tune shift, indicating that the spread of the synchrotron tune was not enlarged. Interestingly, the bunch length remained unchanged below the MWI threshold, as shown in Figs. 8a and 9b. The bunch length were longer when MWI occurred. A more interesting phenomenon is observed when comparing the results shown in Figs. 2a and 7a, indicating a higher TMCI threshold when considering only the real part of the longitudinal impedance. The theory described in Sect. 3 cannot directly explain this phenomenon.

However, the imaginary part of the longitudinal impedance causes bunch lengthening without a centroid shift or driving the MWI. Incoherent tune shifts, and enlargement of the synchrotron-tune spread can also be observed. This phenomenon indicates that the imaginary part of the

longitudinal impedance does not lead to energy loss. Meanwhile, Fig. 9f indicates that the purely imaginary longitudinal impedance causes a significant reduction in the incoherent synchrotron tune and significantly increases the spread of synchrotron tune.

We concluded that the imaginary part of the longitudinal impedance was the main reason for the reduction in the TMCI threshold, and the real part of the longitudinal impedance helped to raise the TMCI threshold.

The analytical method was used to check further the influence of the synchrotron tune conditions on the TMCI threshold. Here, we carried out analytic computations using four different synchrotron-tune situations: the real synchrotron-tune distribution  $v_s(J)$ , unchanged constant synchrotron tune  $v_{s0}$ , average values of the incoherent synchrotron tune  $\langle v_s(J) \rangle$ , and minimum value of the synchrotron tune  $\min(v_s(J))$ . The results are shown in Fig. 10.

Figure 10a shows that the downward shift of  $l=0$  mode is identical regardless of the synchrotron-tune values used. This phenomenon indicates that the frequency of  $l=0$  mode does not depend on the value of synchrotron tune. However, this can also be observed in Fig. 10a, the frequencies of all other modes (except  $l = 0$  mode) are different when different values of the synchrotron tune are used in the computation. By comparing the green, blue, and black dots shown in Fig. 10a, we can see that the coupling between the  $l = 0$  and  $l = -1$  modes occurs at lower single-bunch charges if the synchrotron tune decreases, indicating that the reduction in the synchrotron tune is responsible for the lower threshold. The same conclusion was drawn by comparing the growth rates under different conditions, as shown in Fig. 10b. Furthermore, it can be observed from the red dots in Fig. 10a, the mode-shift trends are different when a synchrotron-tune spread exists. The frequency spread of each mode becomes larger as the bunch charge increases, which suggests that different “modes” couple at lower charges (e.g., lower than 5 nC). The growth rates are shown in Fig. 10b, no significant growth is observed when the bunch charge is lower than approximately 10 nC. This phenomenon is related to the effects of the synchrotron-tune spread on the TMCI threshold, which is left for future study.

### 5 Conclusions and discussions

TMCI is an important single-bunch instability in circular accelerators. Various studies on TMCI have been conducted through analytical methods, simulations, and experiments. Widely used analytical methods to study TMCI involve solving the linearized Vlasov equation. However, previous Vlasov solvers usually do not consider longitudinal impedance, which is not fully self-consistent.

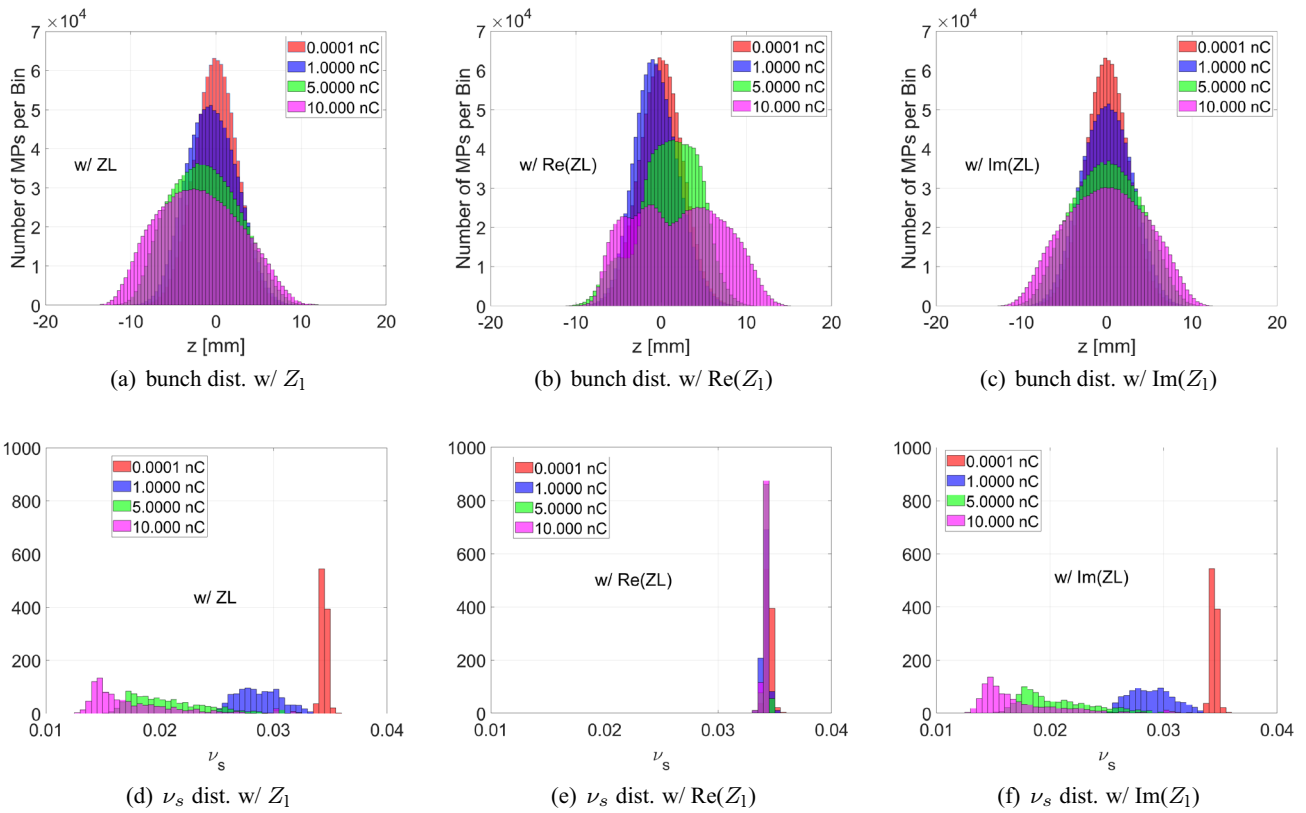


**Fig. 9** (Color online) Distributions of the single bunches and distributions of the synchrotron tune. The three different conditions of longitudinal impedance, which were the condition with longitudinal

impedance (a, d), with only the real part of the longitudinal impedance (b, e) and with only the imaginary part of the longitudinal impedance (c, f), were used in the tracking simulations

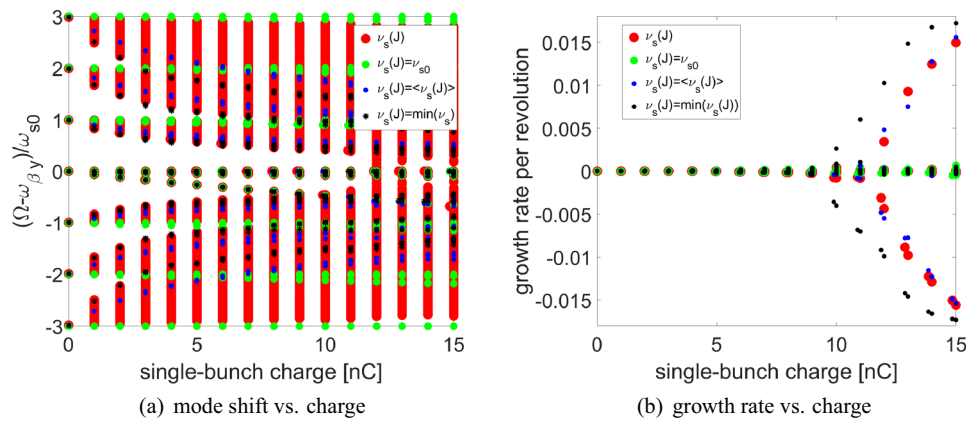


**Fig. 10** (Color online) Comparison of the mode shift and growth rates with the assumption of different synchrotron tune. The red dots represent the results obtained by using the real distribution of synchrotron tune  $\nu_s(J)$ . The results shown by the green, blue, and black dots were obtained, assuming the synchrotron tune was constant. The

green dots, the blue dots, and the black dots represented the results obtained when using the maximum value ( $\max(\nu_s(J)) = \nu_{s0}$ ), the mean value ( $\langle \nu_s(J) \rangle$ ), and the minimum value ( $\min(\nu_s(J))$ ) of  $\nu_s(J)$ , respectively.

Recently, studies on TMCI in FCC-ee reported a lower TMCI threshold current when longitudinal impedance was included in multiparticle tracking simulations. The lower

synchrotron tune caused by the longitudinal impedance was identified as the main reason for the lower TMCI threshold. We conducted similar studies for the CEPC collider ring and

observed a similar phenomenon. To explore the physical picture in detail, we developed an analytical method that includes longitudinal impedance in TMCI computations (inspired by previous work on the beam–beam effect with longitudinal impedance). The key is that we did not assume a linear longitudinal motion. Instead, the distorted phase-space trajectories and corresponding distributions of the synchrotron tune were used as the input information for the code. The Haïssinski solution was used as the equilibrium distribution. However, it should be noted that the equilibrium Haïssinski solution does not always exist. When MWI occurs, the physics indicates that no equilibrium Haïssinski solution exists; therefore, it is not suitable to address situations above the threshold current of the MWI. Multiparticle tracking is suitable in such complicated situations.

In this paper, we present studies of TMCI with longitudinal impedance performed using both the analytic method and multiparticle tracking simulations. The reduction in the incoherent synchrotron tune caused by the imaginary part of the longitudinal impedance was the main reason for the reduction in the TMCI threshold current after considering the longitudinal impedance. However, the real part of the longitudinal impedance increases the TMCI threshold. This conclusion provides clear guidance for the optimization of longitudinal impedance.

**Acknowledgements** The authors thank their colleagues in the Accelerator Physics Group of the IHEP for their fruitful discussions. The author, Chun-Tao Lin, would also like to thank his colleagues at the IASF. Most simulations were performed on a cluster operated by the IHEP Computing Center. The authors appreciate the kind support provided by the staff at the IHEP computing center.

**Author Contributions** All authors contributed to the study conception and design. Material preparation, data collection and analysis were performed by HX, CL, NW, JX and YZ. The first draft of the manuscript was written by HX, and all authors commented on previous versions of the manuscript. All authors read and approved the final manuscript.

**Data availability statement** The data that support the findings of this study are openly available in Science Data Bank at <https://cstr.cn/31253.11.sciencedb.07576> and <https://www.doi.org/10.57760/sciencedb.07576>.

## Declarations

**Conflict of interest** The authors declare that they have no Conflict of interest.

## References

- R.D. Kohaupt, Simplified presentation of head tail turbulence. Technical Report DESY-M-80-19 (1980)
- A.W. Chao, Physics of collective beam instabilities in high energy accelerators, in *Beam Physics and Accelerator Technology*, (Wiley, Hoboken, 1993)
- K. Ohmi, N. Kuroo, K. Oide et al., Coherent beam-beam instability in collisions with a large crossing angle. *Phys. Rev. Lett.* **119**, 134801 (2017). <https://doi.org/10.1103/PhysRevLett.119.134801>
- N. Kuroo, K. Ohmi, K. Oide et al., Cross-wake force and correlated head-tail instability in beam–beam collisions with a large crossing angle. *Phys. Rev. Accel. Beams* **21**, 031002 (2018). <https://doi.org/10.1103/PhysRevAccelBeams.21.031002>
- Y. Zhang, N. Wang, K. Ohmi et al., Combined phenomenon of transverse impedance and beam–beam interaction with large Piwinski angle. *Phys. Rev. Accel. Beams* **26**, 064401 (2023). <https://doi.org/10.1103/PhysRevAccelBeams.26.064401>
- C.T. Lin, K. Ohmi, Y. Zhang, Coupling effects of beam–beam interaction and longitudinal impedance. *Phys. Rev. Accel. Beams* **25**, 011001 (2022). <https://doi.org/10.1103/PhysRevAccelBeams.25.011001>
- M. Borland, Elegant: A flexible SDDS-compliant code for accelerator simulation, in *Advanced Photon Source LS-287*, (Argonne National Laboratory, 2000)
- Y. Wang, M. Borland, Pelegant: A parallel accelerator simulation code for electron generation and tracking, in *Proceedings on 12th Advanced Accelerator Concepts Workshop*, (Vol. 877, 2006), p. 241  
<https://github.com/PyCOMPLETE/PyHEADTAIL>
- G. Skripka, R. Nagaoka, M. Klein et al., Simultaneous computation of intrabunch and interbunch collective beam motions in storage rings. *Nucl. Instrum. Meth. Phys. Res. A* **806**, 221–230 (2016). <https://doi.org/10.1016/j.nima.2015.10.029>
- H.S. Xu, U. Locans, A. Adelmann et al., Calculation of longitudinal collective instabilities with mbrack-cuda. *Nucl. Instrum. Meth. Phys. Res. A* **922**, 345–351 (2019). <https://doi.org/10.1016/j.nima.2019.01.041>
- Y.H. Chin, User's guide for new MOSES version 2.0: MODE-coupling Single bunch instability in an Electron Storage ring, CERN-LEP-TH-88-05 (1988)
- A. Burov, Nested head-tail Vlasov solver. *Phys. Rev. ST Accel. Beams* **17**, 021007 (2014). <https://doi.org/10.1103/PhysRevSTAB.17.021007>
- N. Mounet, Vlasov solvers and macroparticle simulations. CERN Yellow Reports: Conference Proceedings, **1**, CERN-2018-003-CP (2018). <https://cds.cern.ch/record/2674107https://doi.org/10.23732/CYRCP-2018-001.77>
- E. Métral, M. Migliorati, Longitudinal and transverse mode coupling instability: Vlasov solvers and tracking codes. *Phys. Rev. Accel. Beams* **23**, 071001 (2020). <https://doi.org/10.1103/PhysRevAccelBeams.23.071001>
- H.S. Xu, J.Y. Xu, N. Wang, Influences of harmonic cavities on single-bunch instabilities in electron storage rings. *Nucl. Sci. Tech.* **32**, 89 (2021). <https://doi.org/10.1007/s41365-021-00926-7>
- Y. Jiao, G. Xu, X.H. Cui et al., The HEPES project. *J. Synch. Radiat.* **25**, 1611–1618 (2018). <https://doi.org/10.1107/S1600577518012110>
- H.S. Xu, C. Meng, Y.M. Peng et al., Equilibrium electron beam parameters of the high energy photon source. *Radiat. Detect. Technol. Methods* **7**, 279–287 (2023). <https://doi.org/10.1007/s41605-022-00374-w>
- J. Byrd, M. Georgsson, Lifetime increase using passive harmonic cavities in synchrotron light sources. *Phys. Rev. ST Accel. Beams* **4**, 030701 (2001). <https://doi.org/10.1103/PhysRevSTAB.4.030701>
- G.M. Ma, Z.T. Zhao, J.F. Liu, Design of a higher harmonic cavity for the SSRF storage ring. *Chin. Phys. C* **25**, 275 (2008). <https://doi.org/10.1088/1674-1137/32/4/007>
- T. Phimsen, B.C. Jiang, H.T. Hou et al., Improving Touschek lifetime and synchrotron frequency spread by passive harmonic cavity in the storage ring of SSRF. *Nucl. Sci. Tech.* **28**, 108 (2017). <https://doi.org/10.1007/s41365-017-0259-y>

22. M. Venturini, Harmonic cavities and the transverse mode-coupling instability driven by a resistive wall. *Phys. Rev. Accel. Beams* **21**, 024402 (2018). <https://doi.org/10.1103/PhysRevAccelBeams.21.024402>
23. M. Migliorati, C. Antuono, E. Carideo et al., Impedance modeling and collective effects in the future circular  $e^+e^-$  collider with 4 IPs. *EPJ Tech. Instrum.* **9**, 10 (2022). <https://doi.org/10.1140/epjti/s40485-022-00084-z>
24. Y.W. Wang, S. Bai, J. Gao et al., Lattice design of the CEPC collider ring for a high luminosity scheme. in *Proceedings of the 12th International Particle Accelerator Conference, Campinas, SP, Brazil*. <https://jacow.org/ipac2021/papers/wepab033.pdf><https://doi.org/10.18429/JACoW-IPAC2021-WEPAB033>
25. N. Wang, Y. Zhang, H.S. Xu et al., Impedance driven collective effects in CEPC. *J. Instrum.* **19**, P02016 (2024). <https://doi.org/10.1088/1748-0221/19/02/P02016>
26. N. Wang, Q. Qin, Resistive-wall impedance of two-layer tube. *Phys. Rev. ST Accel. Beams* **10**, 111003 (2007). <https://doi.org/10.1103/PhysRevSTAB.10.111003>
27. S.Y. Lee, *Accelerator Physics* (Fourth Edition). (World Scientific, 2019). <https://doi.org/10.1142/11111>
28. K. Oide, a mechanism of longitudinal single bunch instability in storage rings. *Part. Accel.* **51**, 43 (1995)
29. R. Warnock, K. Bane, Numerical solution of the Haissinski equation for the equilibrium state of a stored electron beam. *Phys. Rev. Accel. Beams* **21**, 124401 (2018). <https://doi.org/10.1103/PhysRevAccelBeams.21.124401>
30. R. Warnock, M. Venturini, Equilibrium of an arbitrary bunch train in presence of a passive harmonic cavity: solution through coupled haissinski equations. *Phys. Rev. Accel. Beams* **23**, 064403 (2020). <https://doi.org/10.1103/PhysRevAccelBeams.23.064403>
31. T.L. He, W.W. Li, Z.H. Bai et al., Numerical solution of the coupled Haissinski equations for the equilibrium state of an arbitrary bunch train in an electron storage ring. *Nucl. Instrum. Meth. Phys. Res. A* **1006**, 165434 (2021). <https://doi.org/10.1016/j.nima.2021.165434>
32. A. Wolski, *Beam dynamics in high energy particle accelerators*. World Sci. (2014). <https://doi.org/10.1142/p899>

Springer Nature or its licensor (e.g. a society or other partner) holds exclusive rights to this article under a publishing agreement with the author(s) or other rightsholder(s); author self-archiving of the accepted manuscript version of this article is solely governed by the terms of such publishing agreement and applicable law.